The polymorphs of the Na^+ ion conductor Na_3PS_4 from the perspective of variable temperature diffraction and spectroscopy

Theodosios Famprikis [a,b,†,‡], Houssny Bouyanfif [c], Pieremanuele Canepa [d,e], James A. Dawson [f,g], Mohamed Zbiri [h], Emmanuelle Suard [h], François Fauth [i], Helen Y. Playford [j], Damien Dambournet [k,‡], Olaf J. Borkiewicz [l], Matthieu Courty [a,‡], Jean-Noël Chotard [a,‡], M. Saiful Islam [b,†]* and Christian Masquelier [a,†,‡]**

[a]Laboratoire de Réactivité et Chimie des Solides (LRCS), CNRS UMR 7314, Université de Picardie Jules Verne, 80039 Amiens, France

[b]Department of Chemistry, University of Bath, BA2 7AY, United Kingdom

[c]Laboratoire de Physique de la Matière Condensée (LPMC), UR 2081, Université de Picardie Jules Verne, Amiens 80039, France

[d]Department of Materials Science and Engineering, National University of Singapore, 117576, Singapore

[e]Department of Chemical and Biomolecular Engineering, National University of Singapore, 117585, Singapore

[f]Chemistry—School of Natural and Environmental Sciences, Newcastle University, Newcastle upon Tyne NE1 7RU, United Kingdom

[g]Centre for Energy, Newcastle University, Newcastle upon Tyne, NE1 7RU, United Kingdom

[h]Institut Laue-Langevin (ILL), BP 156, 71 Avenue des Martyrs, 38042 Grenoble, France

[i]CELLS – ALBA Synchrotron, Cerdanyola del Vallès, 08290 Barcelona, Spain ILL

[j]ISIS Facility, Rutherford Appleton Laboratory, Didcot OX11 0QX, United Kingdom

[k]Physico-Chimie des Electrolytes et Nano-systèmes Interfaciaux (PHENIX), CNRS UMR 8234, Sorbonne Université, F-75005 Paris, France

[l]X-ray Science Division, Advanced Photon Source, Argonne National Laboratory, Argonne, Illinois, USA

[†]ALISTORE European Research Institute, CNRS FR 3104, 80039 Amiens, France

[‡]Réseau sur le Stockage Électrochimique de l'Énergie (RS2E), CNRS FR 3459, 80039 Amiens, France

Corresponding Authors

t.famprikis@tudelft.nl ; m.s.islam@bath.ac.uk; christian.masquelier@u-picardie.fr

ABSTRACT: Solid electrolytes are crucial for next-generation solid-state batteries and Na_3PS_4 is one of the most promising Na^+ conductors for such applications. In this contribution, we present a detailed investigation of the evolution in structure and dynamics of Na_3PS_4 under the effect of temperature in the range 30 < T < 600 °C through combined experimental-computational analysis. Although x-ray Bragg diffraction experiments indicate a second-order phase transition from the tetragonal ground state (α, $P\bar{4}2_1c$) to the cubic polymorph (β, $I\bar{4}3m$), pair distribution function analysis in real space and Raman spectroscopy indicate remnants of tetragonal character in the range 250 < T < 500 °C which we attribute to dynamic local tetragonal distortions. The first-order phase transition to the mesophasic high-temperature polymorph (γ, $Fddd$) is associated with a sharp volume increase and the onset of liquid-like diffusive dynamics for sodium-cations (translative) and thiophosphate-polyanions (rotational) evident by inelastic neutron- and Raman- spectroscopies, as well as pair-distribution function and molecular dynamics. These results shed light on the rich polymorphism in Na_3PS_4 and are relevant for a host of high-performance materials deriving from the Na_3PS_4 structural archetype.

INTRODUCTION

Battery technology is the key to the electrification of transport and the integration of renewable energy in the grid. The push to improve on the current state-of-the-art lithium-ion battery technology has converged towards the investigation of various post-lithium-ion concepts; among them solid-state batteries which rely on the substitution of the liquid electrolyte with solid ion-conductors [1,2]. In parallel, economic and geopolitical considerations over the availability of lithium have motivated research on sodium analogues of the lithium(-ion) battery chemistries. The above strategies and their advantages can be combined in solid-state sodium(-ion) batteries which rely on fast Na^+ conductors.

Sodium orthothiophosphate (Na_3PS_4) is the archetypical member of a very promising family of Na^+ conductors, with a distinct crystal structure compared to the compositionally analogous thio-LISICON (e.g. Li_3PS_4) [3]. Notable compositions of the Na_3PS_4 structural family include Na_3SbS_4 with a room-temperature conductivity of the order of 10^{-3} S/cm and distinct stability against ambient moisture, and the recently reported tungsten-doped $Na_{3-x}W_xSb_{1-x}S_4$ with RT Na^+-conductivity of the order of 10^{-2} S/cm [4,5], currently the highest reported among polycrystalline Na^+ and Li^+ conductors.

In recent contributions we have examined the effect of mechanochemical synthesis and pressure application on the room-temperature structure and dynamics of Na_3PS_4 [6] and brought to light a new high-temperature polymorph with plastic crystal characteristics [7]. Here, we explore the evolution in the structure and dynamics of well-crystalline Na_3PS_4 samples with temperature through diffraction (Bragg and pair distribution function), spectroscopy (Raman, inelastic neutron scattering) and associated theoretical analyses with a focus on the accurate description of the nature of the different polymorphs and phase transitions.

RESULTS

The sample investigated in this study is a polycrystalline powder of Na_3PS_4 synthesized through a solid-state route from a stoichiometric mixture of Na_2S and P_2S_5 as first demonstrated by Jansen and Henseler [8] (see Methods).

Diffraction Analysis. Variable temperature Bragg diffraction experiments shown in Figure 1a reveal the evolution of the average structure of Na_3PS_4 in the range 35-550 °C. A smooth, continuous evolution of the diffractograms is observed in the range 35-500 °C corresponding to the α- and β-polymorphs of Na_3PS_4 [8,9]. The characteristic peak merging and extinction of the tetragonal-to-cubic transition is observed in the range 200-300 °C. Above 500 °C Na_3PS_4 transforms into the recently discovered plastic γ-polymorph [7]. Representative fits of the neutron and x-ray Bragg diffractograms for each polymorph are shown in the SI (Figures S1-S3, Tables S1-S3).

The lattice volume, extracted from the diffractogram refinements and plotted in Figure 1b, shows a smooth evolution with temperature in the range 35-500 °C with no discontinuity corresponding to the α-to-β transition. In this temperature range the relationship between molar volume and temperature remains linear with a slight change of slope corresponding to the α-to-β transition. The thermal expansion coefficient calculated for the α-phase from the slope of the V vs. T plot in the range 30-200 °C amounts to ~1.0 x 10^{-4} K^{-1} (referenced to the volume at 30 °C). This value increases slightly upon transition to ~1.1 x 10^{-4} K^{-1} as calculated for the range 300-500 °C (referenced to the volume at 300 °C). In contrast, the β-to-γ transition is associated with large discontinuity in lattice volume involving a sizeable ~10% expansion. The phase transitions and volume evolution are fully reversible on cooling albeit with certain hysteresis on the transition temperatures notably for the γ-to-β transition (Figure S4). In addition, there are some changes in the relative intensities of Bragg peaks of the α- and β-phases on cooling, which we attribute to the anisotropic growth of these phases in preferential orientations upon recrystallization from the γ-phase.

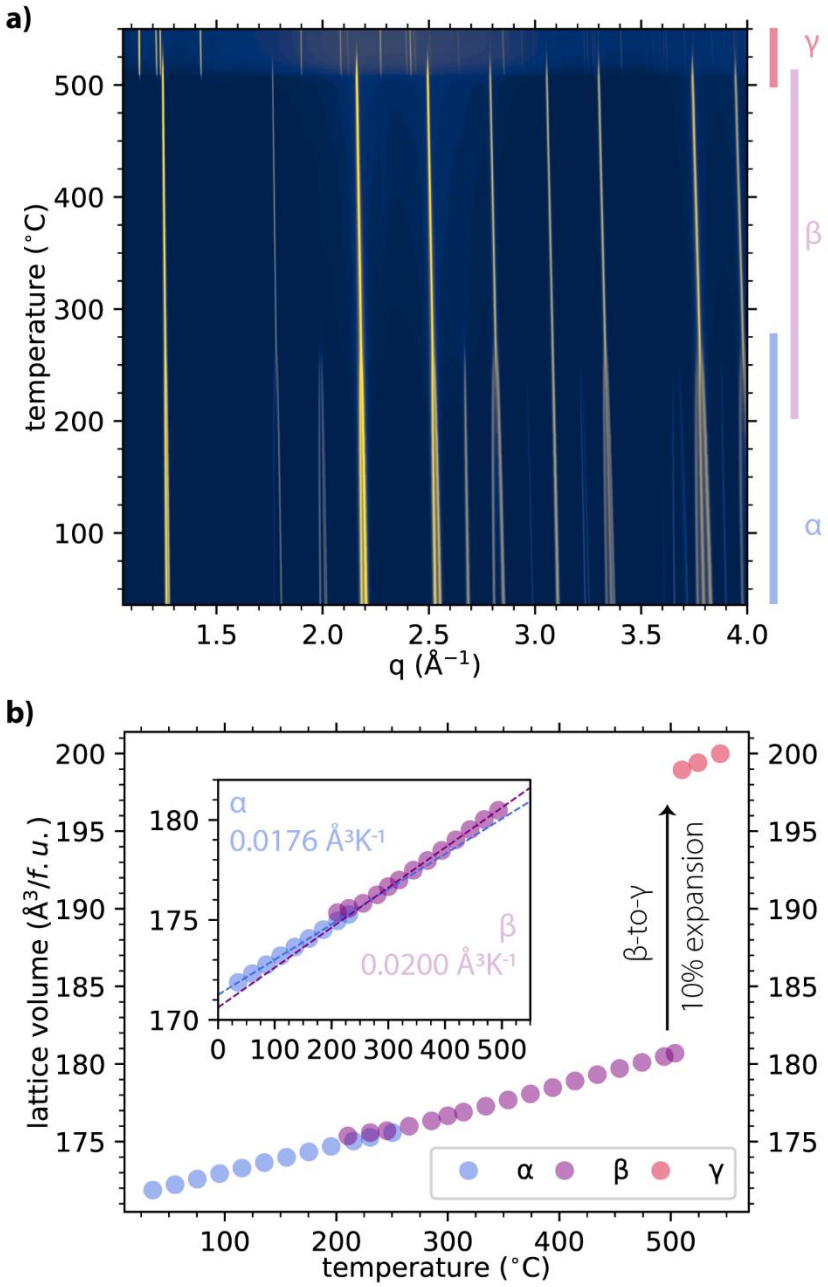

Figure 1: Variable-temperature Bragg diffraction experiments on Na_3PS_4 in the range 35-550 °C. (a) Contour plot of the diffractograms as a function of temperature. (b) Evolution of the crystallographic lattice volume as a function of temperature. Inset: Magnification of the previous panel highlighting a slight change in slope between the cubic and the tetragonal polymorphs. Only a subset of available data points are plotted in (b) for clarity.

We further investigated the evolution of the local structure through total diffraction experiments using x-rays and neutrons. From such experiments we extract the pair distribution function (PDF)

which represents a "weighted histogram of the interatomic distances" in the material. The evolution of the x-ray pair distribution function in the range 30-600 °C is plotted in Figure 2 and annotated with the pairwise interatomic distances corresponding to the room-temperature structure of α-Na_3PS_4.

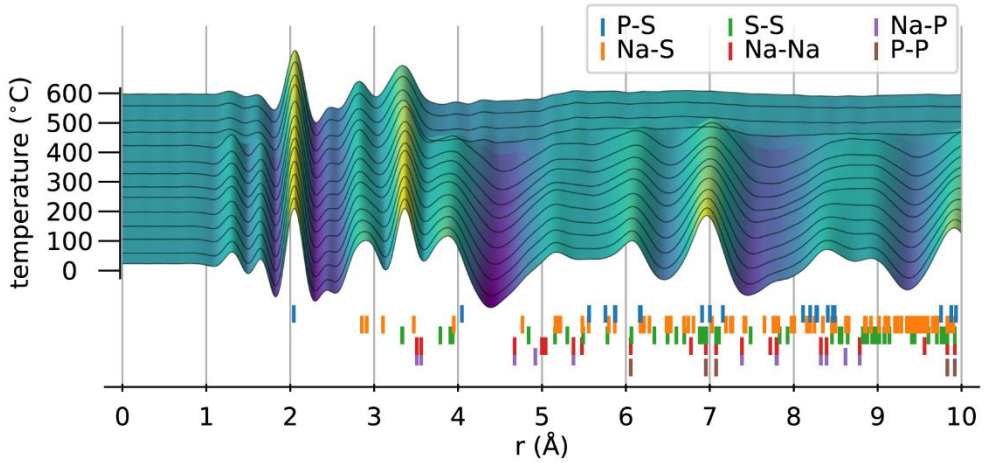

Figure 2: Pair distribution function of Na_3PS_4 in the range 0-10 Å as a function of temperature in the range 30-600 °C. Discreet PDFs shown every ~50 °C. The distances associated with pairwise correlations at 30 °C are identified for reference. Apparent unindexed peaks at 1.4, 1.7 and 2.4 Å are artifacts of the Fourier transform.

Upon heating, most PDF peaks broaden and shift to higher distances continuously, signatures of increased atomic mobility and of the expansion of the crystalline lattice, respectively. No discontinuous change in the local structure can be observed corresponding to the α-to-β transition at ~250 °C. The neutron PDFs of the α and β polymorphs, measured at 30 and 300 °C, respectively, can be well fit through small-box Rietveld-type refinements in the tetragonal $P\bar{4}2_1c$ framework (Figures S5 and S6). On the other hand, most interatomic correlations vanish completely upon the phase transition to the γ-phase, observed here at ~470 °C. Both neutron and x-ray measurements corroborate this observation (Figure S7). Continuous peak broadening is to be expected at higher temperatures from increased thermal motion but the discontinuous vanishing of most peaks indicates a transition to a liquid-like local structure in the γ-phase. The sole peaks that persist beyond the β-to-γ transition are those corresponding to the nearest-neighbor P-S (~2.0 Å), Na-S (~2.8 Å) and S-S (~3.5 Å) atomic pairs. The first-order P-S pair, corresponding to the P-S bond of the PS_4^{3-} anion, is the least affected by the transition: it shows only a slight broadening and,

surprisingly, a slight shift to lower r, in contrast to the expected effect of increasing temperature and discussed further on. Similar observations can be made for the first order S-S pair (intramolecular S-S correlation in the PS_4^{3-} moiety) with an additional distinct broadening, indicating increased vibrational freedom for the PS_4^{3-} moiety.

Vibrational Spectroscopy. The dynamical properties of Na_3PS_4 were investigated by means of variable temperature Raman- and inelastic neutron spectroscopies. To aid in the interpretation of the vibrational spectra, we also performed a group-theoretical analysis to derive the vibrational modes at the Γ-point and subsequently performed DFT-based calculations to simulate the energies of said and approximate Raman intensities of said modes. Figure 3a compares the results of calculations with a Raman spectrum collected at 100 K for increased resolution. The agreement between calculated and experimental spectra is excellent. We underline that the calculated frequencies have not been scaled to fit the experimental data. The spectra are dominated by the normal modes of the PS_4^{3-} anion, denoted ν_1-ν_4, clearly visible above 210 cm^{-1}.

The four normal modes of the ideal (isolated) PS_4 tetrahedron are split into multiple frequencies (degeneracy is lifted), mainly due to the effect of the symmetry reduction in the tetragonal space group [10,11]: In the tetragonal α-polymorph the point group symmetry at the phosphorus site (S_4) and of the unit cell (D_{2d}) are lower than T_d leading to three distinct frequencies for each of the asymmetric ν_3 and ν_4 modes, and to two distinct frequencies of the symmetric bending ν_2 mode ('static field-' or 'site group' splitting [10]). Notably, our theoretical analysis indicates that this effect of mode splitting should be absent in the β-polymorph where both the phosphorus site- and unit cell point group symmetry are T_d as illustrated in Table 1 and elaborated on in the Supporting Information.

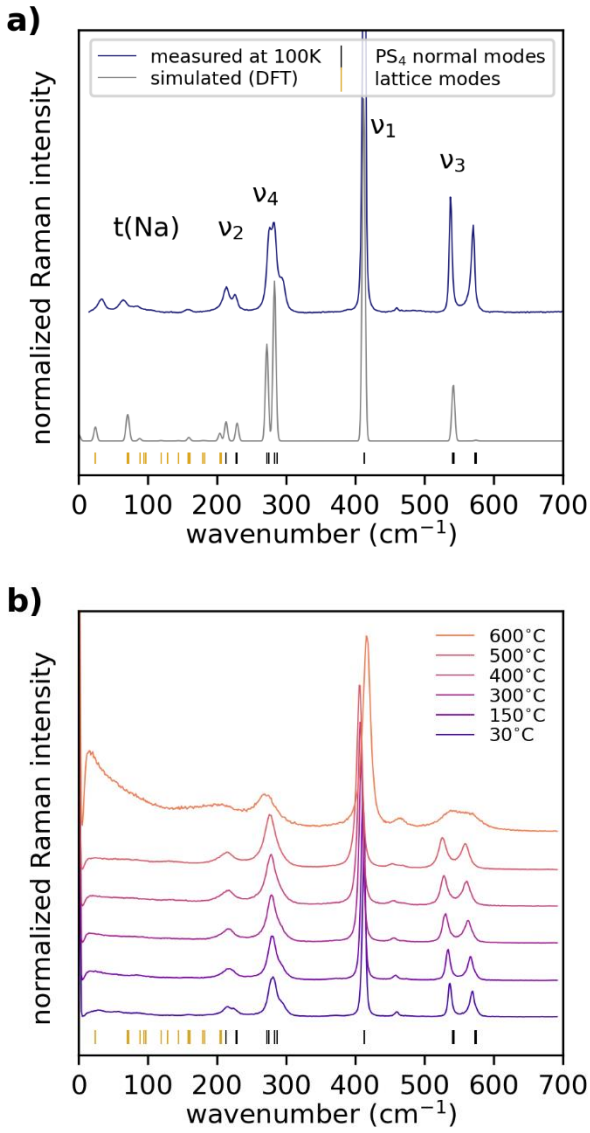

Figure 3: Raman spectra of Na_3PS_4. (a) Comparison of the experimental spectrum measured at 100K and simulated based on DFT. The peak shape of the calculated spectrum is arbitrary. ν_1-ν_4 denotes the normal modes of the PS_4^{3-} tetrahedron and t(Na) represents modes associated with Na^+ translation (b) Evolution of the Raman spectra with temperature in the range 30<T<600 °C.

Table 1: Molecular site group analysis for the PS_4^{3-} anion in (a) α-Na_3PS_4 and (b) β-Na_3PS_4. Correlations between the symmetry of the free PS_4^{3-} anion, the site symmetry of the P atom, and the point group of the unit cell. ν_1-ν_4: normal modes, r: rotation/libration, t: translation.

α-Na_3PS_4 ($P\bar{4}2_1c$)

free ion symmetry $\bar{4}3m$ (T_d)	site symmetry $\bar{4}$ (S_4)	unit cell symmetry $\bar{4}2m$ (D_{2d})
A_1 (ν_1)	3A	$3A_1$
		$3A_2$
E (ν_2)	4B	$4B_1$
T_1 (r)		$4B_2$
T_2 (ν_3, ν_4, t)	4E	8E

β-Na_3PS_4 ($I\bar{4}3m$)

free ion symmetry $\bar{4}3m$ (T_d)	site symmetry $\bar{4}3m$ (T_d)	unit cell symmetry $\bar{4}3m$ (T_d)
A_1 (ν_1)	A_1	A_1
E (ν_2)	E	E
T_1 (r)	T_1	T_1
T_2 (ν_3, ν_4, t)	T_2	T_2

The frequencies of the Raman modes are accurately predicted from calculation; however, there are certain discrepancies between the calculated and observed intensities in Fig. 3a. Most obviously, the intensities of high frequency ν_3 asymmetric stretching modes at 573 and 575 cm^{-1} are significantly underestimated in calculations. Lower-energy modes below 210 cm^{-1} mostly pertain to librations of the PS_4^{3-} anions and to translations of the Na^+ cations (Table 2). Although the intensities of most of these modes are quite low, we can observe a certain few at 100 K and assign them based on the DFT calculations. It is highlighted that these are the modes responsible for carrying the Na^+ ions to the transition states for hopping to occur, i.e. these low energy modes are directly responsible for Na^+ migration in Na_3PS_4. The complete list of vibrational modes including their associated symmetries and comparison with experiment are tabulated in Table 2 for α-Na_3PS_4, with details and the analogous analysis for β-Na_3PS_4 shown in the SI (Tables S6-S12).

Table 2: Full list of vibrational modes of α-Na_3PS_4 including assignments; compared with the modes observable by Raman spectroscopy at 100K. ν_1-ν_4: normal modes, r: rotation/libration, t: translation. e.g r(PS_4 | [001]) rotation of PS_4 about the c-axis; t(Na1 | [100], [010]) translation of Na1 along the a- and b-axes. Modes assigned according to the dominant atomic displacement vectors. Lattice modes (#1-30) sometimes include with a secondary displacement in addition to the main one.

α-Na_3PS_4 ($P\bar{4}2_1c$)				
mode #	calc. freq (cm^{-1})	mode symmetry	exp. freq. (cm^{-1})	mode assignment
1	0	B2	acoustic	t(PS_4,Na1,Na2 | [001], [010])
2-3	0	2xE	acoustic	t(PS_4,Na1,Na2 | [100])
4-5	24	2xE	32	t(Na2 | [100], [010]), r(PS_4 | [100], [010])
6	70	A1	70	t(Na1 | [001]), r(PS_4 | [001])
7-8	72	2xE	84?	t(Na2 | [100], [010])
9	88	B2	84?	t(Na1 | [001])
10-11	94	2xE	not observed	t(PS_4 | [100], [010])
12	97	B1	not observed	t(PS_4 | [001])
13-14	119	2xE	not observed	r(PS_4 | [100], [010]), t(Na2 | [100], [010])
15	128	(A2)	(inactive)	r(PS_4 | [001]), t(Na1 | [001])
16-17	128	2xE	not observed	r(PS_4 | [100], [010]), t(Na2 | [100], [010])
18	144	A1	not observed	r(PS_4 | c), t(Na1 | c)
19-20	158	2xE	not observed	t(Na1, Na2 | [110]), r(PS_4 | [100], [010])
21-22	159	2xE	157?	t(Na2 | [100], [010])
23	161	B1	157?	t(Na1 | [001])
24	174	(A2)	(inactive)	t(Na1 | [001]), r(PS_4 | [001])
25	179	B2	not observed	t(Na2 | [001])
26	182	B1	not observed	t(Na2 | [001])
27-28	204	2xE	not observed	t(Na1, [100], [010])
29-30	206	2xE	not observed	t(Na1, [110])
31-32	213	A1+(A2)	214	ν_2(PS_4) symmetric bend
33	227	B2	226	
34	229	B1	226	
35	272	B2	276	ν_4(PS_4) asymmetric bend
36	275	B1	276	
37-38	283	2xE	283	
39-40	287	2xE	293	
41-42	412	A1+(A2)	413	ν_1(PS_4) symmetric stretch
43	541	B2	537	ν_3(PS_4) asymmetric stretch
44-45	542	2xE	537	
46	573	B1	567	
47-48	575	2xE	570	

At room temperature and above only the normal modes of the PS_4^{3-} are observable in the Raman spectra (Figure 3b). These evolve smoothly with heating, softening (i.e. red-shifting to lower energies/wavenumbers) up to ~550 °C. Most interestingly, the splitting of the normal modes is observed invariantly in the temperature domain of the β-polymorph (250-500 °C) indicating that the local symmetry remains tetragonal and that the $I\bar{4}3m$ average symmetry from Bragg diffraction does not accurately capture the local structure of β-Na_3PS_4. Above 550 °C, a distinct broadening of the peaks is observed along with stepwise shifts in frequency: softening (red-shift) for the ν_2 and ν_4 bending modes (210 and 270 cm^{-1}) and hardening (blue-shift) for the ν_1 and ν_3 stretching modes (~415 and 550 cm^{-1}). The discontinuous peak shifts at ~550 °C are accompanied with a distinct rise of the signal around the elastic peak (E=0). This "broadening of the elastic peak" points to a finite energy process of quasi-elastic nature and can be attributed to atomic mobility of continuous stochastic, non-phonon character (in contrast to discreet lattice excitations). These observations are reversible with hysteresis on cooling and assigned to the β-to-γ phase transition. We note that blue-shifting of molecular internal frequencies is typically characteristic of melting, consistent with the assignment of γ-Na_3PS_4 as a "partially molten" mesophase [7].

Figure 4a presents the generalized phonon density of states (GDOS) of Na_3PS_4 extracted from inelastic neutron scattering (INS) measurements. The GDOS are complementary to the Raman spectra in that they involve a weighting of the scattering ions with their scattering power, resulting in increased sensitivity for the lower energy modes involving Na^+. Moreover, whereas Raman probes uniquely the Γ-point, INS allows the probing of the whole Brillouin zone. The GDOS evolve significantly with temperature with features broadening significantly from RT to 400 °C. The spectra at 550 and 700 °C corresponding to the γ-phase show barely any features. Notably, the low energy (0-5 meV) behavior of the GDOS also significantly changes upon transition to γ-Na_3PS_4. Towards the transition to γ-Na_3PS_4, the Debye growth in the 0-5 meV acoustic region exhibits a clear deviation from a E^2-like behavior possibly reflecting the onset of an amorphous or liquid-like structural component of the molten sublattices. The observed significant broadening of GDOS features with increasing temperature supports this interpretation and can also be considered as a consequence of increased amplitudes of atomic vibrations.

To interpret the measured spectra we have extracted the neutron-weighted phonon density of states (GDOS) from the trajectories of *ab initio* molecular dynamics (MD) simulations of Na_3PS_4 at

300, 500 and 900 K (SI). To facilitate the comparison with the INS data, we consider the specific case at 300K, offering the best peak resolution. The agreement between the measured and calculated GDOS is excellent and as such we use it as a basis to interpret the evolution of the measured spectra with temperature. The phonon spectrum below ~30 meV is dominated by Na and shows distinct broadening with increasing temperature. While modes dominated by Na are well-resolved at RT and 147 °C, they start to broaden upon transition to the β-phase as seen in the 402 °C, spectrum. Mode definition is lost completely upon transition to the γ phase. This reduction in intensity and definition (damping) of the Na modes can be attributed to Na atoms no longer performing oscillatory motions but rather exhibiting long-range diffusion; i.e the Na-dynamics are no longer "phononic-" but rather "diffusive" in nature. Similar arguments can be made for the PS_4^{3-} tetrahedra which likely do not diffuse but undergo "stochastic" rotations. The γ phase is therefore dynamically dominated by continuous motions, akin to a liquid. This interpretation is supported by the observation of a characteristic quasi-elastic signal which will be discussed independently in a forthcoming contribution focused on quasi-elastic neutron scattering (QENS).

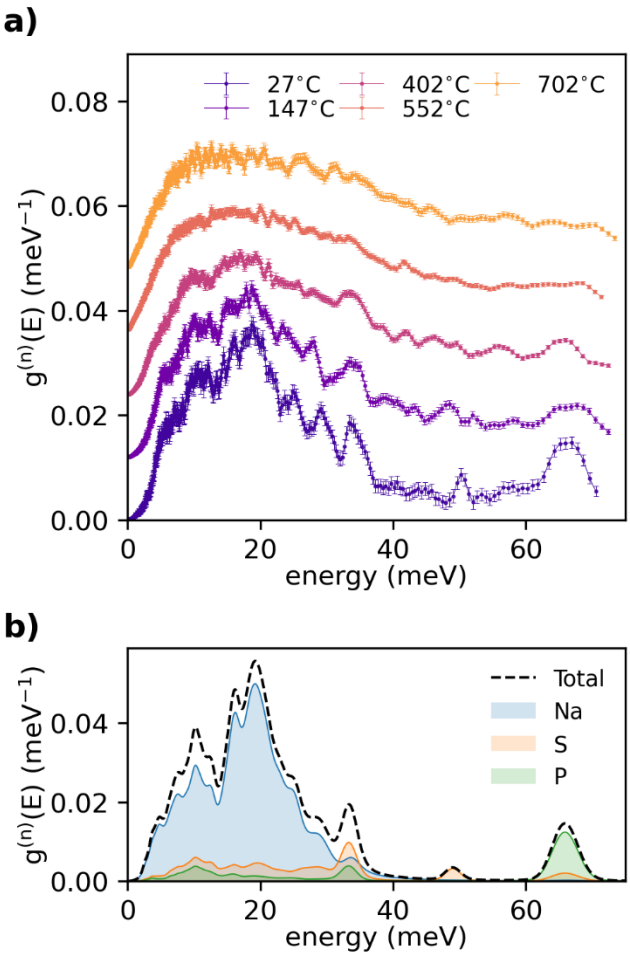

Figure 4. Neutron-weighted phonon density of states $g^{(n)}(E)$ as (a) experimentally measured by INS and (b) extracted from AIMD calculations at 300 K. Spectra in (a) staggered by 0.012 meV^{-1} for clarity.

Thermal Analysis. The thermogram of Na_3PS_4 on heating, shown in Figure 5, reveals a single endothermic effect in the range 30-600°C, with an onset at ~500 °C in agreement with previous measurements[7,8]. Here we performed differential scanning calorimetry, calibrated with a standard sample so that the isobaric heat capacity (c_P) could be quantified. The c_P was determined to be ~1.0 J/(gK) in the range 30-500 °C and ~1.2 J/(gK) for temperatures >520 °C. The small endothermic peak observed at ~460 °C is likely an experimental artifact. Additional DSC experiments were performed using quartz crucibles to avoid reaction with Na_3PS_4 and allow for thermograms up to 800 °C, exhibiting the onset of a large endothermic effect at 765 °C (Figure S8). In parallel, pelletized samples were evacuated in quartz ampules and heated to various temperatures for visual inspection (Figure S9). From these experiments we determine the melting point of Na_3PS_4 as 765 °C; in contrast to the previously cited value of 517 °C [8,12], which actually pertains to the β-to-γ phase transition[7].

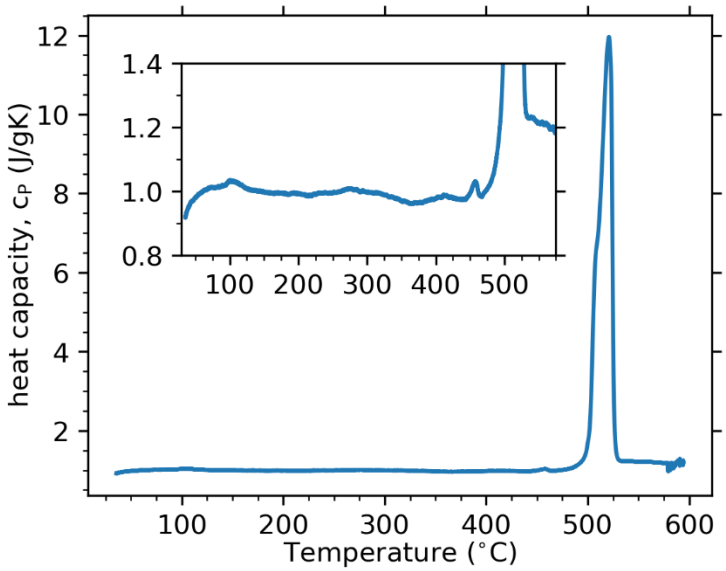

Figure 5: Thermogram of Na_3PS_4 on heating in the range 30-600 °C from differential scanning calorimetry. Inset: magnification of the y-axis showing an increase in the baseline above 500 °C

DISCUSSION

In the following, we use our comprehensive variable-temperature data to classify the phase transitions in Na_3PS_4 and discuss the nature of the high-temperature polymorphs β and γ.

Classification of phase transitions. By definition the Gibbs free energies, G, of two polymorphs are equal at the phase transition temperature (ΔG_{trans}=0). However, the derivatives of G might show discontinuities and phase transitions can be classified with respect to such discontinuities (Ehrenfest classification [13]). Discontinuities in the first derivative of G, i.e. entropy ($S = (\frac{\partial G}{\partial T})_P$) or volume ($V = (\frac{\partial G}{\partial P})_T$), characterize 'first-order' phase transitions. At the phase transition temperature ΔG_{trans}=0; $\Delta H_{trans} = \Delta S_{trans}/T$, so changes in entropy in first-order transitions typically manifest in a latent heat (ΔH) observable in thermal analysis. Similarly, discontinuities in the second derivative of G, i.e. isobaric heat capacity ($c_P = T(\frac{\partial S}{\partial T})_P \propto \frac{d^2G}{dT^2}$), thermal expansion coefficient ($\alpha_V = \frac{1}{V}(\frac{\partial V}{\partial T})_P \propto \frac{d^2G}{dPdT}$), and isothermal compressibility ($\beta_T = -\frac{1}{V}(\frac{\partial V}{\partial P})_T \propto \frac{d^2G}{dP^2}$), denote 'second order' phase transitions and so on.

α-to-β phase transition. As evident from the thermogram of Figure 5, there is no discernible latent heat associated with the α-to-β phase transition in Na_3PS_4, nor a discontinuity in heat capacity. A close group-subgroup relationship exists between the space groups of the two polymorphs, $P\bar{4}2_1c$ and $I\bar{4}3m$, as shown in Table 3. We note that an intermediate body-centered tetragonal group, namely $I\bar{4}2m$, is predicted by crystallographic theory [14], which however, we were not able to unambiguously identify in our experimental diffractograms. Under the heating rate of 5 °C/min utilized in our x-ray Bragg diffraction experiment, a large temperature range of coexistence for the α- and β polymorphs can be observed, spanning roughly 180-280 °C (Figure S10). It is unclear at this point whether this coexistence is due to kinetic effects due to the rapid heating rate or whether a temperature region of thermodynamic equilibrium exists for the two-phase mixture. No discontinuity in volume is observed, but a slight discontinuity in the thermal expansion coefficient is detected (Figure 1b, inset). The PDFs and Raman spectra exhibit a smooth evolution in this range of temperatures indicating no stark change in local structure (Figs. 2 and 3b, respectively).

***Table 3**: Group-subgroup relationship of the different atomic positions in the α- and β-polymorphs of Na_3PS_4. 25%-occupied Na3 offers an alternative description to Na1+Na2 for β-Na_3PS_4*

	α-Na_3PS_4 $P\bar{4}2_1c$ (114)		**$I\bar{4}2m$ (121)**		**β-Na_3PS_4 $I\bar{4}3m$ (217)**	
Atom	**Wyckoff**	**Point Grp.**	**Wyckoff**	**Point Grp.**	**Wyckoff**	**Point Grp.**
P	2a (0, 0, 0)	$\bar{4}$	2a (0, 0, 0)	$\bar{4}2m$	2a (0, 0, 0)	$\bar{4}3m$
S	8e (x, y, z)	1	8i (x, x, z)	$..m$	8c (x, x, x)	$.3m$
Na1	4d (0, ½, z)	2	4c (0, ½, 0)	222	6b (0, ½, ½)	$\bar{4}2m$
Na2	2b (0, 0, ½)	$\bar{4}$	2b (0, 0, ½)	$\bar{4}2m$		
(Na3)			$8g_1$ (x_1, 0, ½) $8g_2$ (x_2, 0, ½) 8h (0, ½, z)	.2 . .2 . 2..	24f (x, ½, 0)	2..

Figure 6 schematically depicts the slight structural differences in the structures of the α and β-polymorphs of Na_3PS_4. We note that the model for the β-phase shown here includes a single Na atom at the 6b position for simplicity, in contrast to the ¼-occupied 24f site that results in slightly better fits of the Bragg diffractograms. For the transition to occur it is necessary for Na atoms to translate and for the PS_4 units to slightly rotate. Namely, the 4d Na atoms in α-Na_3PS_4 need to slide along the c-axis (so that their z=0, see Table 1). The PS_4 rotation also happens about the c-axis, i.e. the S atoms coherently shift in the ab plane. Through these subtle translations and the convergence of the lattice parameters the average symmetry is increased from tetragonal to cubic upon heating.

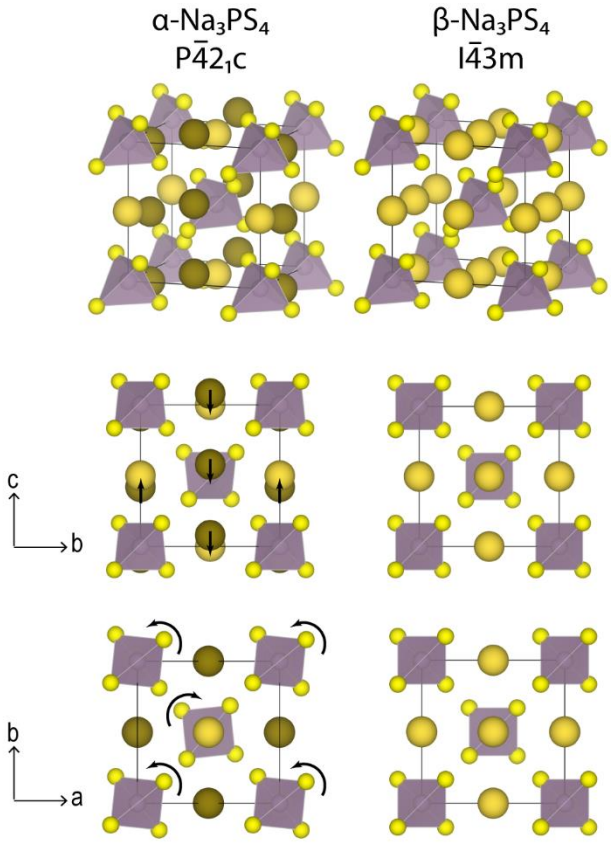

Figure 6: *Structural relationship between α and β-Na_3PS_4. The transition occurs upon translation of the 4d Na atoms (highlighted in brown) and rotation of the PS_4 tetrahedra about the c-axis. These atomic displacements are associated with the soft mode observable at 70 cm^{-1} in the Raman spectra.*

We underline that these exact atomic displacements associated with the α-to-β phase transition constitute a specific vibrational mode at the Γ-point: mode #6 in Table 2; observable at 70 cm^{-1} in the Raman spectra of Figure 3a); however, the resolution of our Raman measurements do not allow

us to track the evolution of this mode around the α-to-β transition temperature. Furthermore, model calculations of the Raman spectra of the β-polymorph ($I\bar{4}3m$) in the primitive setting (two formula units) result in a shift of this mode to negative frequencies, confirming the dynamic instability of the β-polymorph at oK.

From the ensemble of these observations, namely no discontinuity in the first derivatives of free energy (V,S) and a slight discontinuity in the second derivative (α_V) we characterize the α-to-β transition in Na_3PS_4 as one of weak second-order. Furthermore, given that the atomic displacements of Na and S are responsible for the transition (Figure 6) we characterize it as displacive. We note that previous theoretical work has shown that the α-to-β transition can also be brought about by applied pressure, which is consistent with the lower lattice volume exhibited by β-Na_3PS_4 stabilized at room-temperature through mechanochemistry[6]. Thus, overall, increasing temperature and increasing pressure both favor the higher-average-symmetry β-phase.

It is then of interest to discuss the nature of the β-phase, especially in view of practical applications, as it had been shown that this middle-temperature phase could be stabilized at ambient conditions by mechanochemistry resulting in elevated Na^+ conductivity compared to the α-phase [15,16]. We have thoroughly examined these mechanochemical effects in an earlier contribution where we in fact detected no significant difference in local structure between the ball-milled- and high-temperature-synthesized samples beyond a notable macro- and micro-strain imparted on the former from the harsh mechanochemical synthesis conditions [6].

In considering a well-crystalline β-Na_3PS_4 sample at 300 °C in the present study, similar observations can be made: the local structure experimentally observed by PDF can be better described in small-box, Rietveld-type simulations in the $P\bar{4}2_1c$ space-group, indicating a similar tetragonal local structure to the room temperature α-phase. The Raman spectra show no discontinuity upon transition to the β-phase and the mode splitting associated to the tetragonal distortion (static field splitting) persist, showing no indication of a more symmetric environment

for the PS_4^{3-} polyanions, as implied by the $I\bar{4}3m$ description [i]. The only concrete evidence of a phase transition stems from Bragg diffraction, where a convergence of the lattice parameters to a cubic cell are clearly observed.

This set of observations leads us to describe β-Na_3PS_4 as a 'pseudo-cubic' polymorph, closely related to the tetragonal ground state α-Na_3PS_4. We hypothesize that these seemingly contrasting observations can be reconciled by an increased atomic mobility in β-Na_3PS_4, namely translational for the Na^+ and rotational for the PS_4^{3-}. In the cubic long-range framework, such atomic mobility can lead to localized tetragonal distortions which could explain the PDF and Raman spectroscopic findings, as previously hypothesized in relation to room-temperature-stabilized samples of β-Na_3PS_4 [6,17,18]. Such tetragonal distortions are exactly the displacements (translations and rotations) shown in Figure 6 and could be static or dynamic in nature, the differentiation between which should be the subject of further study. It is likely that the distribution of such tetragonal domains within crystallites of β-Na_3PS_4 is dynamically evolving at high temperatures (250-500 °C) and "frozen" for samples stabilized at RT, e.g. by mechanochemistry or quenching. This interpretation, is supported by the refinement of our neutron PDF at 300 °C as shown in Figure 7a. The refined anisotropic displacement parameters for Na and S, visualized in Figure 7b,c, show direct evidence of the atomic translations associated with the tetragonal distortion in Figure 6, namely along the c axis for Na and in the ab plane for S.

[i] We note that, in principle, mode splitting could also originate from dynamical coupling of the vibrations of the neighboring PS_4^{3-} anions ('correlation field-'or 'factor group' splitting) [10]. Still, this alternative interpretation is also not coherent with the cubic description of the β-polymorph as discussed in the Supporting Information.

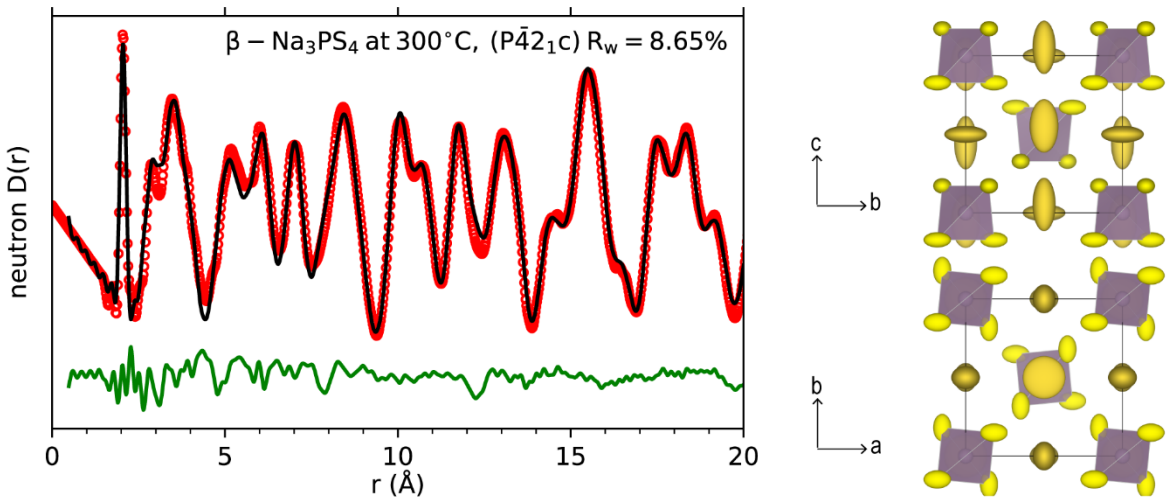

Figure 7: *Neutron PDF of Na_3PS_4 at 300 °C. (a) Small-box Rietveld-type fit to the data in the range 0.5-20 Å in the tetragonal $P\bar{4}2_1c$ space group. (b), (c) Visualizations of the refined structure projected in the bc and ab planes, respectively. Ellipsoids drawn at 75% probability. The displacements of Na1 and S correspond exactly to the α-to-β phase transition in Na_3PS_4*

These observations on the nature of the β-polymorph of Na_3PS_4 likely also apply to the isostructural Na_3PnX_4 (Pn: P, As, Sb; X: S, Se) which all exhibit analogous α-β polymorphism. The selenides Na_3PSe_4 and Na_3SbSe_4 actually exhibit the β-phase at ambient temperature (their corresponding α-to-β transition temperatures are approximately -30 and -80 °C, respectively[19]). Indeed, the Raman spectra of the β-polymorphs of Na_3PSe_4 and Na_3SbSe_4 show the same signs of tetragonal local structure through splitting of the ν_3 modes [19–21] as shown here for Na_3PS_4.

β-to-γ phase transition. The high temperature γ-phase is indexed in space group *Fddd* which bears no group-subgroup relationship with those of the two lower temperature polymorphs. Although the β-phase continues to be observable in Bragg diffractograms in the range 500-540 °C, its lattice parameters cease to evolve in this temperature range. The observable coexistence of β- and γ- is likely owing to the fast heating rate of the Bragg diffraction experiments (5 °C/min) in conjunction with the slower kinetics of the β-to-γ transition compared to the α-to-β one. A large discontinuity in volume is observed, along with a discontinuity in the thermal expansion coefficient. In contrast to the α-to-β transition, the β-to-γ is associated with a large latent heat of ~150 J/g and a change in heat capacity from ~1.0 to ~1.2 J/(gK). In addition, since at the transition temperature $\Delta G_{trans}=0$, we can estimate the entropy change of transition as $\Delta S_{trans}=\Delta H_{trans}/T_{trans}=0.19$ J/(gK). A strong hysteresis of the transition temperature is observed in all

experiments conducted on cooling (Bragg diffraction, Raman spectroscopy, DSC). From the ensemble of these observations, namely strong discontinuities in the first derivatives of free energy (V,S) and no obvious structural relation to the lower-temperature polymorphs, we conclude that the β -to-γ transition in Na_3PS_4 is of reconstructive nature and thermodynamically of first-order character.

We have posited in a previous contribution that γ-Na_3PS_4 is a mesophasic material of plastic crystalline nature[7] and the additional data presented here support that description. The Raman spectra at high temperatures indicate isolated PS_4^{3-} tetrahedra in a liquid-like environment. Both the Raman and inelastic neutron spectra indicate the breakdown of phononic quasi-particles for Na-dominated modes in favor of stochastic, "non-phononic" behavior, again indicative of a molten Na sublattice. The Lorentzian broadening of the central peaks in both these inelastic scattering techniques indicate fast diffusive behavior likely attributed to both the Na^+ and PS_4^{3-} (translational and rotational, respectively).

Both Raman and PDF coherently expose a counterintuitive evolution of the P-S covalent bonds upon transition to the γ-phase. Namely, the P-S bond shortens and stiffens (Figure 8), in contrast to the typical trends upon heating of solid materials. This increased internal interaction in the PS_4^{3-} moiety could be understood through decreased interaction between PS_4^{3-} and Na^+, i.e. the melting of the Na^+ sublattice. In other words, the electronic density around the sulfur atoms shifts from coordinating the Na^+ ions to the P-S covalent bonds. We note that the transition temperature varies significantly between experiments (~550 °C for Raman, ~470 °C for PDF, ~500 °C for DSC and Bragg diffraction); we tentatively ascribe these discrepancies to the different temperature control setups, heating rates and sample amounts inherent to the different techniques.

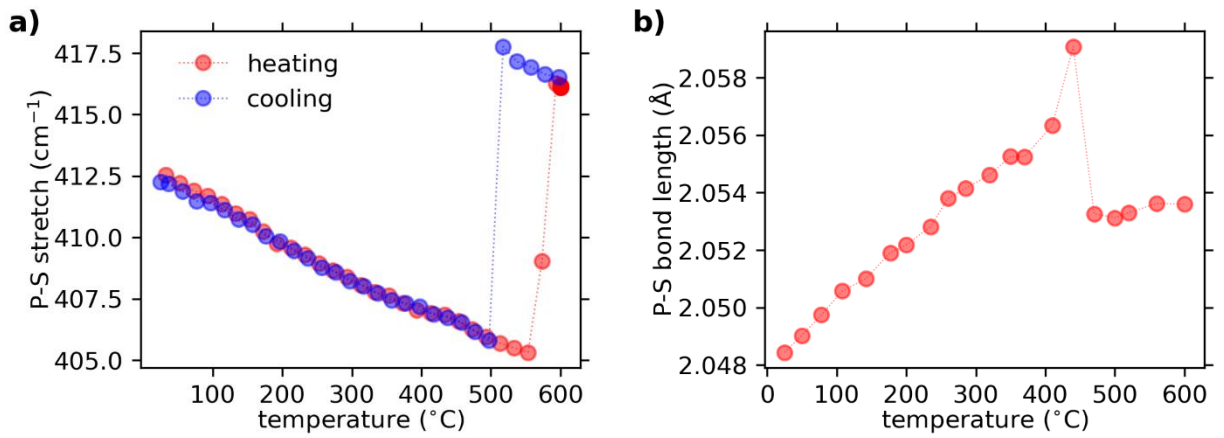

Figure 8: Evolution of the P-S bond with temperature (a) evolution of the P-S stretching (ν_1) frequency with temperature from Raman spectroscopy (b) evolution of the P-S (bond) length with temperature from PDF.

In addition, the pair distribution function of γ-Na_3PS_4 indicates no strong interatomic correlations beyond the first neighbor P-S, Na-S and S-S pairs, reminiscent of amorphous or liquid systems. This might appear counter-intuitive, given the distinct Bragg reflections exhibited by γ-Na_3PS_4, clearly indicating a macroscopically solid crystalline material (Figure 9a). We have verified these observations against our ab-initio molecular dynamics simulations published previously[7]. As shown in Figure 9b, the experimental and simulated PDFs are in excellent agreement. This same feature of a liquid-like PDF was also reported recently in independent classical MD investigations of γ-Na_3PS_4 by Sau and Ikeshoji [22].

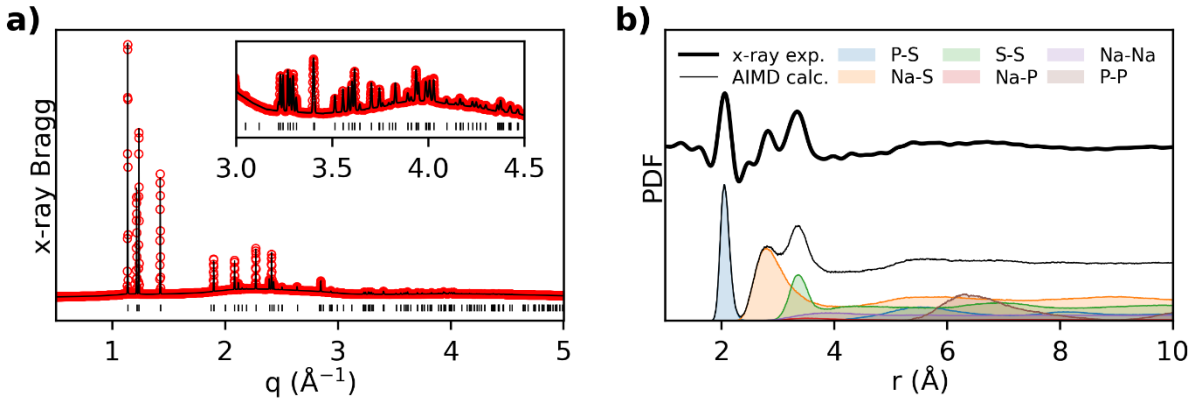

Figure 9: *Diffraction analysis of γ-Na_3PS_4 (a) Bragg diffractogram at 550 °C indexed in the Fddd space group and (b) comparison of pair distribution functions as experimentally measured using x-rays at 600 °C and extracted from ab-initio molecular dynamics simulations at 900 K.*

The combination of sharp Bragg reflections (long-range order) and a "flat" PDF (no short-range correlations) might seem counter-intuitive, but is perfectly in-line with the "plastic" nature of the crystal and highlights the different information accessible by Bragg and total-scattering analyses [23]. The time-averaged centers of mass of the PS_4^{3-} and of the Na probability density are periodically arranged and define the average motif that gives rise to long-range symmetry and Bragg reflections. The sharp P-S and S-S peaks in the PDF elucidate that the PS_4^{3-} moves as a rigid unit, i.e. the material remains an ionic molecular crystal of Na^+ and PS_4^{3-}. At the same time, individual PS_4^{3-} tetrahedra can adopt a multitude of orientations, unconstrained by the orientation of their neighboring tetrahedra. This is captured in the PDF, where, e.g. 2nd P-S neighbor and the first P-P neighbor distances between tetrahedra, nominally at ~5.5 and ~6.5 Å, respectively, are so variable between different "instantaneous snapshots" that said peaks are remarkably broadened and not distinguishable in the total PDF. The distinct asymmetry in first Na-S peak at ~2.8 Å. indicates that Na is not so much "bonded" to the sulfur but rather sterically limited in its liquid-like diffusion by the position of sulfur, i.e. it cannot approach closer than ~2.7 Å. The Na-Na radial distribution function (RDF) is remarkably broad and featureless indicating liquid-like distibution with no correlation. This feature of a liquid-like broad Na-Na radial distribution was also confirmed in the MD studies of Sau and Ikeshoji [22] and is in direct contrast to sharp RDF peaks around 3.5 Å in the case of the α- and β-polymorphs [24,25] where Na is relatively constrained at fully occupied lattice sites.

Another interesting point to discuss pertains to the apparent "symmetry lowering" upon the β-to-γ phase transition. It is hard to unambiguously quantify the "amount of symmetry" between two space groups not related by group-subgroup relationships, as is the case here. Still, from the point of view of symmetry operations per cell volume, the orthorhombic $Fddd$ is clearly of lower symmetry than the cubic $I\bar{4}3m$. Why would then a high-temperature, high-disorder polymorph exhibit lower symmetry?

It seems that the melting of the Na-ion sublattice destabilizes a bcc-like arrangement of PS_4^{3-} units as found in the β-polymorph and the "liquid" Na-sublattice seems to dictate a more complex arrangement of the PS_4^{3-} anions as exhibited in the larger orthorhombic cell. Viewed from another perspective, it is possible that the higher volume required by the highly-mobile Na sublattice cannot

be accommodated in the body-centered cell; note that the first Na-Na RDF peak at ~3.5 Å for the α- and β- phases while ~4 Å for the γ. It is noted that thermograms of the Na_3PS_4-isostructural Na_3SbS_4, Na_3PSe_4 and Na_3SbSe_4 (not shown here) do not indicate the presence of a γ-Na_3PS_4-type plastic polymorph before melting. These isostructures exhibit significantly larger volumes per Na compared to Na_3PS_4 which could be the reason why they can accommodate the increased mobility of Na up to the melting point without breaking the bcc-like arrangement of their respective tetrahedral polyanions.

To our knowledge the case of γ-Na_3PS_4 is unique with respect to its crystal structure; most of the immediately comparable molecular crystal compounds characterized by rotational disorder of their constituent tetrahedral polyanions exhibit full cubic symmetry $Fm\bar{3}m$ (e.g. α-Li_2SO_4, ref. [26]; γ-Na_3PO_4, refs. [27,28]; γ-$Na_4Zn(PO_4)_2$, ref. [29], α-$NaBH_4$, refs. [30,31]). Nevertheless, an analogy can be found in the surprising observations of $Fddd$ symmetry in the seemingly unrelated systems of block copolymer melts; i.e. polymers of two or more different monomers arranged in a linear fashion along the polymer chain. These systems present a host of mesophases between their liquid and solid forms and recently, self-assemblies of AB diblock-[32–36] and ABC triblock [37–39] copolymer melts have been observed to exhibit $Fddd$ symmetry. Although these structures present the $Fddd$ symmetry on a much larger scale (of the order of 10nm; observable by small-angle diffraction) a number of similarities indicate a fundamental connection between them and γ-Na_3PS_4. Namely, theoretical and experimental analyses converge to the ideal ratio of orthorhombic unit cell of dimensions approaching a:b:c = $1 : 2 : 2\sqrt{3}(\approx 3.46)$ for such mesophases, which is very close to what we observe for γ-Na_3PS_4 (1 : 1.8 : 3.2). These systems are mesophasic, with properties in between solid and liquid, and exhibit remarkable mobility of their constituent atoms. In a recent theoretical investigation it was shown that such $Fddd$ mesophases could be stabilized even in single-component systems in which case the diffusivity of constituent particles was practically identical to that of the liquid phase [40]. These $Fddd$ mesophases were shown to be stable at specific volume ratios between the different block copolymers or, equivalently at a specific density for the single-component systems [40]; which by analogy lends weight to our hypothesis that steric considerations are the key parameter in the stability of γ-Na_3PS_4.

CONCLUSION

We have reported here a thorough variable-temperature analysis of Na_3PS_4 through diffraction (Bragg, PDF) and spectroscopy (Raman, INS). We demonstrate that such a multi-technique approach is critical for the accurate interpretation of often-contrasting observations regarding the polymorphs of Na_3PS_4. Our results converge in the characterization of the α-to-β transition at ~250 °C as a weakly second-order, displacive phase transition and the β-to-γ transition at ~500 °C as a first-order reconstructive phase transition. We have accurately determined the thermal expansion coefficient (10^{-4} K^{-1} at RT) and isobaric heat capacity (~1.0 $Jg^{-1}K^{-1}$) as well as the melting point (765 °C) of Na_3PS_4. Our combined diffraction-spectroscopy analysis indicates that the β-phase, although cubic on the average scale, is characterized by a tetragonal local structure through (likely dynamic) subtle displacements of the Na and S atoms. The γ-polymorph is shown to be mesophasic, with properties between solid and liquid, combining strong Bragg diffraction and a featureless pair distribution function.

METHODS

Synthesis. Na_3PS_4 was synthesized by a solid-state synthesis route as first reported by Jansen and Henseler[8]. Stoichiometric ratios of the binary reagents Na_2S and P_2S_5 (Sigma-Aldrich, utilized as received) were intimately mixed first in a mortar pestle and then in a ball-mill jar (typically 5g of precursors with 25 10-mm ZrO_2 balls in an 80 ml ZrO_2 jar, milled for 12 h at 500 rpm). The resulting powder was pelletized and placed in carbon-coated quartz tubes. The carbon-coating of the tubes was achieved by acetone pyrolysis and subsequent annealing at 1000 °C for 12 h under Ar. The quartz tubes were then flame-sealed under vacuum (~10^{-2} mbar) and placed in a furnace for reaction. The temperature of the furnace was slowly increased to 500 °C at 1 °C/min, held for 20 h and naturally cooled to room temperature. The products after synthesis were milled by pestle and mortar into fine powders for further analysis. All handling was performed in Ar-filled gloveboxes.

Bragg diffraction. X-ray powder Bragg diffraction experiments were performed at the BL04-MSPD beamline [41,42] of the ALBA synchrotron in Barcelona, Spain. Samples were flame-sealed in Ar-filled 1-mm-diameter quartz capillaries. Diffractograms were collected in transmission geometry, using the position-sensitive detector MYTHEN and a wavelength of 0.8262 Å, selected using a Si 111 reflection double crystal monochromator. The temperature of the sample was controlled using a hot air blower, calibrated using the thermal expansion of a standard Si sample. Short measurements (30 s) were continuously recorded on heating and cooling from room temperature to 550 °C and back, at a rate of 5 °/min. Longer measurement (270 s) were taken at 30, 300, 500 and 550 °C for refinement.

Neutron powder Bragg diffraction experiments were performed at the D2B beamline of the Institut Laue-Langevin (ILL) in Grenoble, France. Samples (~2 g) were sealed in cylindrical vanadium containers, which were then put inside a vacuum furnace connected to a secondary pump (~10^{-5} mbar). Diffractograms were collected in transmission geometry, using 128 ^{3}He counting tubes and a wavelength of 1.594 Å selected using the (335) reflection of Ge[115] monochromators. Measurements of ~4-6h were taken at 30 and 300 °C.

The analysis of the Bragg diffraction data was performed using the programs in the Fullprof and Jana 2006 software suites[43,44]. The background was defined as a linear interpolation between manually selected points. Le Bail fits were performed to describe the peak broadening using the Thompson-Cox-Hastings pseudo-Voigt function [45] (convoluted with the instrumental resolution in

the case of x-rays). In subsequent Rietveld analyses, occupancies were fixed to the Na_3PS_4 stoichiometry and atomic positions and displacement parameters were fitted.

Total scattering. X-ray total scattering experiments were performed at the 11-ID-B beamline of the Advanced Photon Source at Argonne National Laboratory using high energy x-rays (λ = 0.21130 Å) for high values of momentum transfer (Q = 24.5 $Å^{-1}$). Samples were flame-sealed under Ar in quartz capillaries. The temperature of the sample during measurement was controlled using a hot-air blower. One dimensional diffraction data were obtained by integrating the raw 2D total scattering data in Fit2D. Pair distribution functions (PDFs) were extracted from the background- and Compton scattering-corrected data following Fourier transform using PDFgetX2[46].

Neutron total scattering experiments were performed at the POLARIS beamline of the ISIS neutron source. Powder samples (~2.5 g) were loaded into cylindrical vanadium containers and sealed using copper rings under Ar in a glovebox, which were then put inside a vacuum furnace connected to a secondary pump. Measurements were taken at 30, 300 and 600 °C for 8, 8 and 10 hours respectively. The total scattering data were normalized, corrected for non-sample scattering and Fourier transformed to produce pair distribution functions (PDF) using the program GudrunN[47].

The analysis of the neutron PDFs at 30 and 300 °C was performed using the PDFfit2 engine as implemented in PDFgui[46]. Structural refinements were limited to single unit cells (no supercells) and constrained by the space group symmetry observed in Bragg diffraction ($P\bar{4}2_1c$ or $I\bar{4}3m$). The following parameters were refined in this order: (1) scale factor, (2) peak broadening parameter with 1/r dependence, δ_1 (3) lattice parameters, (4) atomic positions, (5) thermal displacement parameters. The instrumental resolution parameters Q_{damp} and Q_{broad} were set at 0.01 and 0.03 as determined from measurement of a silicon standard.

The quality of each refinement is quantified by the reliability factor weighted R-value, R_w, which describes the difference between the experimental data (obs) and the fit (calc) each data point:

$$R_w = \sqrt{\frac{\sum_{i=1}^{N} w(r_i)[G_{obs}(r_i) - G_{calc}(r_i)]^2}{\sum_{i=1}^{N} w(r_i) G_{obs}^2(r_i)}}$$

with G_{obs} and G_{calc} being the observed and calculated PDF and $w(r_i)$ the weight for each data point.

Raman spectroscopy. The samples used for Raman spectroscopy were prepared identically to the x-ray diffraction samples; i.e. flame-sealed in Ar-filled 1-mm-diameter quartz capillaries. Spectra were measured using a Renishaw inVia Qontor confocal microscope equipped with a 532 nm laser excitation source. The sealed capillary was placed on a temperature-controlled stage (HFS600E-PB4, Linkam) for variable temperature experiments. Cooling was achieved using water or nitrogen flow for temperatures above and below ambient, respectively. Spectra were collected in backscattering geometry using a Centrus detector in the range -750-750 cm^{-1} centered around the elastic peak (Stokes and anti-Stokes). Typically, spectra were continuously measured at a rate of 1 spectrum/minute while heating/cooling at 5 °C/min. The incident power of the laser was set to 5 mW focused by a 10x objective to a spot of about 10 μm on the sample. These parameters were optimized to maximize the signal-over-noise ratio while avoiding excessive local heating and decomposition/melting of the sample.

Inelastic neutron scattering. Samples (~ 2 g) for inelastic neutron scattering (INS) measurements were lightly compacted into pellets and sealed in 10-mm diameter SiO_2 ampules under vacuum (~10^{-2} mbar). The ampules were placed in custom made Nb holders and subsequently in an evacuated furnace environment. Spectra were measured using the cold-neutron, time-of-flight, time-focusing, IN6 spectrometer at the Institut Laue-Langevin (ILL) in Grenoble, France. An incident wavelength of 5.12 Å was used, offering an elastic energy resolution of ~ 0.1 meV, as determined from a standard vanadium sample. The vanadium sample was also used to calibrate the detectors. The measurements were carried out in the high-resolution, inelastic time focusing mode. The phonon spectra were collected in the up-scattering, neutron energy-gain mode up to 80 meV in terms of the generalized density of states (GDOS). In contrast to the vibrational density of states, the GDOS involves a weighting of the scatterers (ions) with their scattering powers σ/M (σ: neutron scattering cross section, M: mass). The values of 0.143, 0.107 and 0.032 barns·amu^{-1} were used for Na, P and S, respectively. Data reduction and treatment, including detector efficiency calibration and background subtraction, were performed using standard ILL procedures implemented in the large array manipulation program (LAMP) package[48]. Data reduction included measuring an identical empty SiO_2 ampule and Nb container under the same experimental conditions. The Q-averaged, multiphonon-corrected[49] GDOS, $g^{(n)}(E)$, was obtained within the incoherent approximation framework[50].

Thermal analysis. For determination of the heat capacity (c_P), three differential scanning calorimetry (DSC) measurements were performed using a Netzsch DSC 204 F1 calorimeter in the range 30-600 °C at a heating rate of 10 °C/min. The blank signal was measured using two empty crucibles. A sapphire reference sample was measured using the same parameters followed by the Na_3PS_4 sample. The samples were placed in aluminium pans with pierced lids. The specific heat capacity (in $Jg^{-1}K^{-1}$) was determined according to the ASTM E1269 protocol according to:

$$c_P{}^{sample} = \frac{DSC^{sample} - DSC^{blank}}{m^{sample} \cdot HR \cdot sensitivity}$$

where DSC is the measured signal (in µV), m is the sample mass (mg), HR the heating rate (K/s), and sensitivity (µV/mW) is defined by the reference measurement and the known heat capacity of sapphire:

$$sensitivity = \frac{DSC^{sapphire} - DSC^{blank}}{m^{sapphire} \cdot HR \cdot c_P{}^{sapphire}}$$

For measurements up to 800°C thermogravimetric analysis (TGA) and differential scanning calorimetry measurements were performed simultaneously using a Netzsch Simultaneous thermal analyzer STA449F3 housed in an Ar-filled glovebox (Jacomex). Samples were placed on quartz holders to avoid reactions at temperatures >600 °C. The measurements were performed under flow of argon gas (60 ml/min) at a heating/cooling rate of 5 °C/min. Oxygen impurities in the argon gas were captured at temperatures of >300 °C by a metallic zirconium ring placed in-line before the sample.

Ab initio molecular dynamics simulation. Calculations in this work were carried out using density functional theory (DFT) with the Vienna ab initio simulation package (VASP) [51]. A plane-wave cut-off energy of 400 eV was utilized for the AIMD calculations. The projector augmented wave method[52] and the PBEsol exchange-correlation functional[53] were employed. The k-space was sampled using the gamma-point only with a 3x3x3 supercell of the α-Na_3PS_4 structure containing 432 atoms and a 3x2x1 supercell of the γ-Na_3PS_4 structure [7] containing 384 atoms. No Na vacancies were added to the supercells. The AIMD simulations were carried out at 300 and 500 K in the α phase and at 900 K in the γ-phase, with a time step of 2 fs. Statistical properties were obtained from >100 ps simulations at 300 K, >72 ps at 500K and >62 ps at 900K, using the NVT ensemble with a Nose–Hoover thermostat[54].

Radial distribution function calculations. Pair radial distribution functions were extracted from the present AIMD simulations on α-Na_3PS_4 and previously reported simulations on γ-Na_3PS_4 [7] in order to compare with the experimentally measured PDFs. The calculation of the RDFs was performed using the g(r) GUI as implemented in the Visual Molecular Dynamics (VMD) suite[55].

GDOS spectra calculations. The partial atomistic vibrational densities of states were extracted from the AIMD simulations on α-Na_3PS_4 (300 and 500 K) and γ-Na_3PS_4 (900 K) by performing a Fourier transform of the velocity autocorrelation function[56] of the trajectories of the different atom types (Na, P and S). In order to compare directly with our INS-derived GDOS spectra, the calculated partial vibrational contributions of the different atoms were neutron weighted to get the total calculated GDOS, $g^{(n)}(E)$. In contrast to the vibrational density of states, the GDOS involves a weighting of the scatterers (ions) with their scattering powers σ/M (σ: neutron scattering cross section, M: mass). The values of 0.143, 0.107 and 0.032 barns·amu^{-1} were used for Na, P and S, respectively.

Vibrational spectra calculations. The vibrational spectra of the various phases of Na_3PS_4 were simulated using density functional theory (DFT) as implemented in the all-electron code CRYSTAL17 [57,58] where the crystalline wavefunctions are expanded as a linear combination of atomic orbitals and further expanded by a consistent triple-ζ plus polarization basis-set[59,60]. The DFT total energy during the geometry relaxation and in the phonon calculations, was converged within ~10^{-10} a.u. and integrated over a well converged and symmetrized 8×8×8 *k*-point mesh. Forces and stresses were converged using the default convergence criteria. Whenever possible, the internal symmetry was maintained. The unknown exchange-correlation contribution to the total energy was approximated by hybrid functional that combines combining the PBE generalized gradient functional by Perdew, Burke and Ernzerhof [61] with a predefined amount of exact exchange (25%) as proposed by Adamo and Barone [62,63]. The truncation of the (infinite) Coulomb and exchange series was set by the tolerances (TOLINTEG): 10^{-7}, 10^{-7}, 10^{-7}, 10^{-9} and 10^{-30} a.u., while a XXLGRID was used for the integration of the charge density. Raman frequencies of the two polymorphs were computed at the **Γ**-point only, employing the finite difference method. Thus, the dynamical matrix was developed using a step size of 0.003 Å for each displacement. The Raman intensities discussed in the manuscript were computed via the Coupled-Perturbed Kohn–Sham method [64,65].

ACKNOWLEDGEMENTS

The authors are grateful to the Institut Laue-Langevin (ILL) for providing beam time on the D2B diffractometer for the powder diffraction measurements and the IN6 spectrometer for the inelastic neutron scattering (INS) measurements; to the ALBA synchrotron for providing beam time on the MSPD diffractometer for powder diffraction measurements; to the Argonne National Laboratory (ANL) for providing beam time on the 11-ID-B beamline of the Advanced Photon Source (APS) for the powder total scattering measurements; and to the ISIS neutron and muon source for providing beam time on the POLARIS diffractometer for powder total scattering measurements[66].

T. F. is thankful to the ALISTORE ERI and the German Academic Exchange Service (DAAD) for funding in the form of PhD scholarships. J.A.D. and M.S.I. gratefully acknowledge the EPSRC Programme Grant EP/M009521/1 for funding and the MCC/Archer consortium (EP/L000202/1) for computational resources. J.A.D. also gratefully acknowledges Newcastle University for funding through a Newcastle Academic Track (NUAcT) Fellowship. P. C. acknowledges funding from the National Research Foundation under his NRFF NRFF12-2020-0012 and the ANR-NRF NRF2019-NRF-ANR073 Na-MASTER. This research used resources of the Advanced Photon Source, a U.S. Department of Energy (DOE) Office of Science User Facility operated for the DOE Office of Science by Argonne National Laboratory under Contract No. DE-AC02-06CH11357.

REFERENCES

(1) Famprikis, T.; Canepa, P.; Dawson, J. A.; Islam, M. S.; Masquelier, C. Fundamentals of Inorganic Solid-State Electrolytes for Batteries. *Nat. Mater.* **2019**, *18*, 1278–1291. https://doi.org/10.1038/s41563-019-0431-3.

(2) Janek, J.; Zeier, W. G. A Solid Future for Battery Development. *Nat. Energy* **2016**, *1*, 16141. https://doi.org/10.1038/nenergy.2016.141.

(3) Kudu, Ö. U.; Famprikis, T.; Fleutot, B.; Braida, M.-D.; Le Mercier, T.; Islam, M. S.; Masquelier, C. A Review of Structural Properties and Synthesis Methods of Solid Electrolyte Materials in the Li_2S–P_2S_5 Binary System. *J. Power Sources* **2018**, *407*, 31–43. https://doi.org/10.1016/j.jpowsour.2018.10.037.

(4) Fuchs, T.; Culver, S. P.; Till, P.; Zeier, W. G. Defect-Mediated Conductivity Enhancements in $Na_{3-x}Pn_{1-x}W_xS_4$ (Pn = P, Sb) Using Aliovalent Substitutions. *ACS Energy Lett.* **2020**, *5*, 146–151. https://doi.org/10.1021/acsenergylett.9b02537.

(5) Hayashi, A.; Masuzawa, N.; Yubuchi, S.; Tsuji, F.; Hotehama, C.; Sakuda, A.; Tatsumisago, M. A Sodium-Ion Sulfide Solid Electrolyte with Unprecedented Conductivity at Room Temperature. *Nat. Commun.* **2019**, *10*, 5266. https://doi.org/10.1038/s41467-019-13178-2.

(6) Famprikis, T.; Kudu, Ö. U.; Dawson, J. A.; Canepa, P.; Fauth, F.; Suard, E.; Zbiri, M.; Dambournet, D.; Borkiewicz, O. J.; Bouyanfif, H.; et al. Under Pressure: Mechanochemical Effects on Structure and Ion Conduction in the Sodium-Ion Solid Electrolyte Na_3PS_4. *J. Am. Chem. Soc.* **2020**. https://doi.org/10.1021/jacs.0c06668.

(7) Famprikis, T.; Dawson, J. A.; Fauth, F.; Clemens, O.; Suard, E.; Fleutot, B.; Courty, M.; Chotard, J.-N.; Islam, M. S.; Masquelier, C. A New Superionic Plastic Polymorph of the Na^+ Conductor Na_3PS_4. *ACS Mater. Lett.* **2019**, *1*, 641–646. https://doi.org/10.1021/acsmaterialslett.9b00322.

(8) Jansen, M.; Henseler, U. Synthesis, Structure Determination, and Ionic Conductivity of Sodium Tetrathiophosphate. *J. Solid State Chem.* **1992**, *99*, 110–119. https://doi.org/10.1016/0022-4596(92)90295-7.

(9) Nishimura, S.; Tanibata, N.; Hayashi, A.; Tatsumisago, M.; Yamada, A. The Crystal Structure and Sodium Disorder of High-Temperature Polymorph β-Na_3PS_4. *J. Mater. Chem. A* **2017**, *5*, 25025–25030. https://doi.org/10.1039/C7TA08391B.

(10) Poulet, H. .; Mathieu, J. P. *Vibration Spectra and Symmetry of Crystals*; Gordon & Breach: New York, 1976.

(11) Rousseau, D. L.; Bauman, R. P.; Porto, S. P. S. Normal Mode Determination in Crystals. *J. Raman Spectrosc.* **1981**, *10*, 253–290. https://doi.org/10.1002/jrs.1250100152.

(12) Blachnik, R.; Rabe, U. Das Thermische Verhalten Der Mischungen Na_2S-P_4S_{10} Und $Na_4Ge_4S_{10}$-P_4S_{10} Des Systems Na_2S-GeS_2-P_4S_{10}. *Zeitschrift für Anorg. und Allg. Chemie* **1980**, *462*, 199–206. https://doi.org/10.1002/zaac.19804620122.

(13) Jaeger, G. The Ehrenfest Classification of Phase Transitions: Introduction and Evolution. *Arch. Hist. Exact Sci.* **1998**, *53*, 51–81. https://doi.org/10.1007/s004070050021.

(14) Seidel, S.; Zeier, W. G.; Pöttgen, R. The Polymorphs of the Na^+ Ion Conductor Na_3PS_4 Viewed from the Perspective of a Group-Subgroup Scheme. *Zeitschrift für Krist. - Cryst. Mater.* **2020**, *235*, 1–6. https://doi.org/10.1515/zkri-2019-0053.

(15) Hayashi, A.; Noi, K.; Sakuda, A.; Tatsumisago, M. Superionic Glass-Ceramic Electrolytes for Room-Temperature Rechargeable Sodium Batteries. *Nat. Commun.* **2012**, *3*, 856. https://doi.org/10.1038/ncomms1843.

(16) Hayashi, A.; Noi, K.; Tanibata, N.; Nagao, M.; Tatsumisago, M. High Sodium Ion Conductivity of Glass–Ceramic Electrolytes with Cubic Na_3PS_4. *J. Power Sources* **2014**, *258*, 420–423. https://doi.org/10.1016/j.jpowsour.2014.02.054.

(17) Krauskopf, T.; Culver, S. P.; Zeier, W. G. Local Tetragonal Structure of the Cubic Superionic Conductor Na 3 PS 4. *Inorg. Chem.* **2018**, *57*, 4739–4744. https://doi.org/10.1021/acs.inorgchem.8b00458.

(18) Takeuchi, S.; Suzuki, K.; Hirayama, M.; Kanno, R. Sodium Superionic Conduction in Tetragonal Na_3PS_4. *J. Solid State Chem.* **2018**, *265*, 353–358. https://doi.org/10.1016/j.jssc.2018.06.023.

(19) Pompe, C. Strukturchemie Und Elektrische Leitfähigkeiten von Natriumchalkogenometallaten, Universität Regensburg, 2016.

(20) Krauskopf, T.; Muy, S.; Culver, S. P.; Ohno, S.; Delaire, O.; Shao-Horn, Y.; Zeier, W. G. Comparing the Descriptors for Investigating the Influence of Lattice Dynamics on Ionic Transport Using the Superionic Conductor Na3PS4-XSex. *J. Am. Chem. Soc.* **2018**, *140*, 14464–14473. https://doi.org/10.1021/jacs.8b09340.

(21) Zhang, L.; Yang, K.; Mi, J.; Lu, L.; Zhao, L.; Wang, L.; Li, Y.; Zeng, H. Na_3PSe_4: A Novel Chalcogenide Solid Electrolyte with High Ionic Conductivity. *Adv. Energy Mater.* **2015**, *5*, 2–6. https://doi.org/10.1002/aenm.201501294.

(22) Sau, K.; Ikeshoji, T. Origin of Fast Ion Conduction in Na 3 PS 4 : Insight from Molecular Dynamics Study. *J. Phys. Chem. C* **2020**, *124*, 20671–20681. https://doi.org/10.1021/acs.jpcc.0c04476.

(23) Funnell, N. P.; Dove, M. T.; Goodwin, A. L.; Parsons, S.; Tucker, M. G. Local Structure Correlations in Plastic Cyclohexane—a Reverse Monte Carlo Study. *J. Phys. Condens. Matter* **2013**, *25*, 454204. https://doi.org/10.1088/0953-8984/25/45/454204.

(24) Dawson, J. A.; Canepa, P.; Clarke, M. J.; Famprikis, T.; Ghosh, D.; Islam, M. S. Toward Understanding the Different Influences of Grain Boundaries on Ion Transport in Sulfide and Oxide Solid Electrolytes. *Chem. Mater.* **2019**, *31*, 5296–5304. https://doi.org/10.1021/acs.chemmater.9b01794.

(25) De Klerk, N. J. J.; Wagemaker, M. Diffusion Mechanism of the Sodium-Ion Solid Electrolyte Na_3PS_4 and Potential Improvements of Halogen Doping. *Chem. Mater.* **2016**, *28*, 3122–3130. https://doi.org/10.1021/acs.chemmater.6b00698.

(26) Nilsson, L.; Thomas, J. O.; Tofield, B. C. The Structure of the High-Temperature Solid Electrolyte Lithium Sulphate at 908K. *J. Phys. C Solid State Phys.* **1980**, *13*, 6441–6451. https://doi.org/10.1088/0022-3719/13/35/004.

(27) Wiench, D. M.; Jansen, M. Über Na_3PO_4: Versuche Zur Reindarstellung, Kristallstruktur Der Hochtemperaturform. *Zeitschrift für Anorg. und Allg. Chemie* **1980**, *461*, 101–108. https://doi.org/10.1002/zaac.19804610116.

(28) Harrison, R. J.; Putnis, A.; Kockelmann, W. Phase Transition Behaviour and Equilibrium Phase Relations in the Fast-Ion Conductor System Na_3PO_4–Na_2SO_4. *Phys. Chem. Chem. Phys.* **2002**, *4*, 3252–3259. https://doi.org/10.1039/b110947b.

(29) Saha, S.; Rousse, G.; Courty, M.; Shakhova, Y.; Kirsanova, M.; Fauth, F.; Pomjakushin, V.; Abakumov, A. M.; Tarascon, J. M. Structural Polymorphism in Na 4 Zn(PO 4) 2 Driven by Rotational Order–Disorder Transitions and the Impact of Heterovalent Substitutions on Na-Ion Conductivity. *Inorg. Chem.* **2020**, acs.inorgchem.0c00612. https://doi.org/10.1021/acs.inorgchem.0c00612.

(30) Soldate, A. M. Crystal Structure of Sodium Borohydride. *J. Am. Chem. Soc.* **1947**, *69*, 987–988. https://doi.org/10.1021/ja01197a002.

(31) Abrahams, S. C.; Kalnajs, J. The Lattice Constants of the Alkali Borohydrides and the Low-Temperature Phase of Sodium Borohydride. *J. Chem. Phys.* **1954**, *22*, 434–436. https://doi.org/10.1063/1.1740085.

(32) Kim, M. I.; Wakada, T.; Akasaka, S.; Nishitsuji, S.; Saijo, K.; Hasegawa, H.; Ito, K.; Takenaka, M. Stability of the Fddd Phase in Diblock Copolymer Melts. *Macromolecules* **2008**, *41*, 7667–7670. https://doi.org/10.1021/ma801268d.

(33) Miao, B.; Wickham, R. A. Fluctuation Effects and the Stability of the Fddd Network Phase in Diblock Copolymer Melts. *J. Chem. Phys.* **2008**, *128*. https://doi.org/10.1063/1.2827472.

(34) Im Kim, M.; Wakada, T.; Akasaka, S.; Nishitsuji, S.; Saijo, K.; Hasegawa, H.; Ito, K.; Takenaka, M. Determination of the FDDD Phase Boundary in Polystyrene-Block-Polyisoprene Diblock Copolymer Melts. *Macromolecules* **2009**, *42*, 5266–5271. https://doi.org/10.1021/ma900205s.

(35) Yamada, K.; Nonomura, M.; Ohta, T. Fddd Structure in AB-Type Diblock Copolymers. *J. Phys. Condens. Matter* **2006**, *18*. https://doi.org/10.1088/0953-8984/18/32/L03.

(36) Takenaka, M.; Wakada, T.; Akasaka, S.; Nishitsuji, S.; Saijo, K.; Shimizu, H.; Kim, M. I.; Hasegawa, H. Orthorhombic Fddd Network in Diblock Copolymer Melts. *Macromolecules* **2007**, *40*, 4399–4402. https://doi.org/10.1021/ma070739u.

(37) Tyler, C. A.; Morse, D. C. Orthorhombic Fddd Network in Triblock and Diblock Copolymer Melts. *Phys. Rev. Lett.* **2005**, *94*, 1–4. https://doi.org/10.1103/PhysRevLett.94.208302.

(38) Bailey, T. S.; Hardy, C. M.; Epps, T. H.; Bates, F. S. A Noncubic Triply Periodic Network Morphology in Poly(Isoprene- b -Styrene- b -Ethylene Oxide) Triblock Copolymers. *Macromolecules* **2002**, *35*, 7007–7017. https://doi.org/10.1021/ma011716x.

(39) Epps, T. H.; Cochran, E. W.; Hardy, C. M.; Bailey, T. S.; Waletzko, R. S.; Bates, F. S. Network Phases in ABC Triblock Copolymers. *Macromolecules* **2004**, *37*, 7085–7088. https://doi.org/10.1021/ma0493426.

(40) Agosta, L.; Metere, A.; Oleynikov, P.; Dzugutov, M. Self-Assembly of a Triply Periodic Continuous Mesophase with Fddd Symmetry in Simple One-Component Liquids. *J. Chem. Phys.* **2020**, *152*, 191101. https://doi.org/10.1063/5.0006096.

(41) Fauth, F.; Peral, I.; Popescu, C.; Knapp, M. The New Material Science Powder Diffraction Beamline at ALBA Synchrotron. *Powder Diffr.* **2013**, *28*, S360–S370. https://doi.org/10.1017/S0885715613000900.

(42) Fauth, F.; Boer, R.; Gil-Ortiz, F.; Popescu, C.; Vallcorba, O.; Peral, I.; Fullà, D.; Benach, J.; Juanhuix, J. The Crystallography Stations at the Alba Synchrotron. *Eur. Phys. J. Plus* **2015**, *130*, 160. https://doi.org/10.1140/epjp/i2015-15160-y.

(43) Rodríquez-Carvajal, J.; Roisnel, T. Line Broadening Analysis Using FullProf*: Determination of Microstructural Properties. *Mater. Sci. Forum* **2004**, *443–444*, 123–126.

https://doi.org/10.4028/www.scientific.net/MSF.443-444.123.

(44) Petrícek, V.; Dušek, M.; Palatinus, L. Crystallographic Computing System JANA2006: General Features. *Zeitschrift fur Krist.* **2014**, *229*, 345–352. https://doi.org/10.1515/zkri-2014-1737.

(45) Thompson, P.; Cox, D. E.; Hastings, J. B. Rietveld Refinement of Debye–Scherrer Synchrotron X-Ray Data from Al_2O_3. *J. Appl. Crystallogr.* **1987**, *20*, 79–83. https://doi.org/10.1107/S0021889887087090.

(46) Farrow, C. L.; Juhas, P.; Liu, J. W.; Bryndin, D.; Božin, E. S.; Bloch, J.; Proffen, T.; Billinge, S. J. L. PDFfit2 and PDFgui: Computer Programs for Studying Nanostructure in Crystals. *J. Phys. Condens. Matter* **2007**, *19*, 335219. https://doi.org/10.1088/0953-8984/19/33/335219.

(47) Soper, A. K. GudrunN and GudrunX Programs: Programs for Correcting Raw Neutron and x-Ray Diffraction Data to Differential Scattering Cross Section. *Rutherford Applet. Lab. Tech. Reports* **2011**, *RAL-TR-201*.

(48) Richard, D.; Ferrand, M.; Kearley, G. J. Analysis and Visualisation of Neutron-Scattering Data. *J. Neutron Res.* **1996**, *4*, 33–39. https://doi.org/10.1080/10238169608200065.

(49) Sjolander, A. Multi-Phonon Processes in Slow Neutron Scattering by Crystals. *Ark. Fys.* **1958**, *14*.

(50) Skold, K.; Price, D. *Neutron Scattering, Volume 23A*; Academic Press, 1986.

(51) Kresse, G.; Furthmüller, J. Efficient Iterative Schemes for Ab Initio Total-Energy Calculations Using a Plane-Wave Basis Set. *Phys. Rev. B* **1996**, *54*, 11169–11186. https://doi.org/10.1103/PhysRevB.54.11169.

(52) Blöchl, P. E. Projector Augmented-Wave Method. *Phys. Rev. B* **1994**, *50*, 17953–17979. https://doi.org/10.1103/PhysRevB.50.17953.

(53) Perdew, J. P.; Ruzsinszky, A.; Csonka, G. I.; Vydrov, O. A.; Scuseria, G. E.; Constantin, L. A.; Zhou, X.; Burke, K. Restoring the Density-Gradient Expansion for Exchange in Solids and Surfaces. *Phys. Rev. Lett.* **2008**, *100*, 136406. https://doi.org/10.1103/PhysRevLett.100.136406.

(54) Evans, D. J.; Holian, B. L. The Nose–Hoover Thermostat. *J. Chem. Phys.* **1985**, *83*, 4069–4074. https://doi.org/10.1063/1.449071.

(55) Humphrey, W.; Dalke, A.; Schulten, K. VMD: Visual Molecular Dynamics. *J. Mol. Graph.* **1996**, *14*, 33–38. https://doi.org/10.1016/0263-7855(96)00018-5.

(56) Dickey, J. M.; Paskin, A. Computer Simulation of the Lattice Dynamics of Solids. *Phys. Rev.* **1969**, *188*, 1407–1418. https://doi.org/10.1103/PhysRev.188.1407.

(57) Dovesi, R.; Erba, A.; Orlando, R.; Zicovich-Wilson, C. M.; Civalleri, B.; Maschio, L.; Rérat, M.; Casassa, S.; Baima, J.; Salustro, S.; et al. Quantum-Mechanical Condensed Matter Simulations with CRYSTAL. *Wiley Interdiscip. Rev. Comput. Mol. Sci.* **2018**, *8*, e1360. https://doi.org/10.1002/wcms.1360.

(58) Dovesi, R.; Saunders, V. R.; Roetti, C.; Orlando, R.; Zicovich-Wilson, C. M.; Pascale, F.; Civalleri, B.; Doll, K.; Harrison, N. M.; Bush, I. J.; et al. *CRYSTAL17. User's Manual*; University of Torino: Torino, 2018.

(59) Laun, J.; Vilela Oliveira, D.; Bredow, T. Consistent Gaussian Basis Sets of Double- and Triple-Zeta Valence with Polarization Quality of the Fifth Period for Solid-State Calculations. *J. Comput. Chem.* **2018**, *39*, 1285–1290. https://doi.org/10.1002/jcc.25195.

(60) Peintinger, M. F.; Oliveira, D. V.; Bredow, T. Consistent Gaussian Basis Sets of Triple-Zeta Valence with Polarization Quality for Solid-State Calculations. *J. Comput. Chem.* **2013**, *34*, 451–459. https://doi.org/10.1002/jcc.23153.

(61) Perdew, J. P.; Burke, K.; Ernzerhof, M. Generalized Gradient Approximation Made Simple. *Phys. Rev. Lett.* **1996**, *77*, 3865–3868. https://doi.org/10.1103/PhysRevLett.77.3865.

(62) Perdew, J. P.; Ernzerhof, M.; Burke, K. Rationale for Mixing Exact Exchange with Density Functional Approximations. *J. Chem. Phys.* **1996**, *105*, 9982–9985. https://doi.org/10.1063/1.472933.

(63) Adamo, C.; Barone, V. Toward Reliable Density Functional Methods without Adjustable Parameters: The PBE0 Model. *J. Chem. Phys.* **1999**, *110*, 6158–6170. https://doi.org/10.1063/1.478522.

(64) Ferrero, M.; Rérat, M.; Kirtman, B.; Dovesi, R. Calculation of First and Second Static Hyperpolarizabilities of One- to Three-Dimensional Periodic Compounds. Implementation in the CRYSTAL Code. *J. Chem. Phys.* **2008**, *129*, 244110. https://doi.org/10.1063/1.3043366.

(65) Maschio, L.; Kirtman, B.; Rérat, M.; Orlando, R.; Dovesi, R. Ab Initio Analytical Raman Intensities for Periodic Systems through a Coupled Perturbed Hartree-Fock/Kohn-Sham Method in an Atomic Orbital Basis. I. Theory. *J. Chem. Phys.* **2013**, *139*, 164101. https://doi.org/10.1063/1.4824442.

(66) Masquelier, C.; Morisset, A.; Smith, R.; Playford, H.; Famprikis, T. Elucidation of Dynamic Structural Characteristics of γ-Na_3PS_4 Plastic Crystal through Neutron-PDF. STFC ISIS Neutron and Muon Source 2019. https://doi.org/10.5286/ISIS.E.RB2000052.